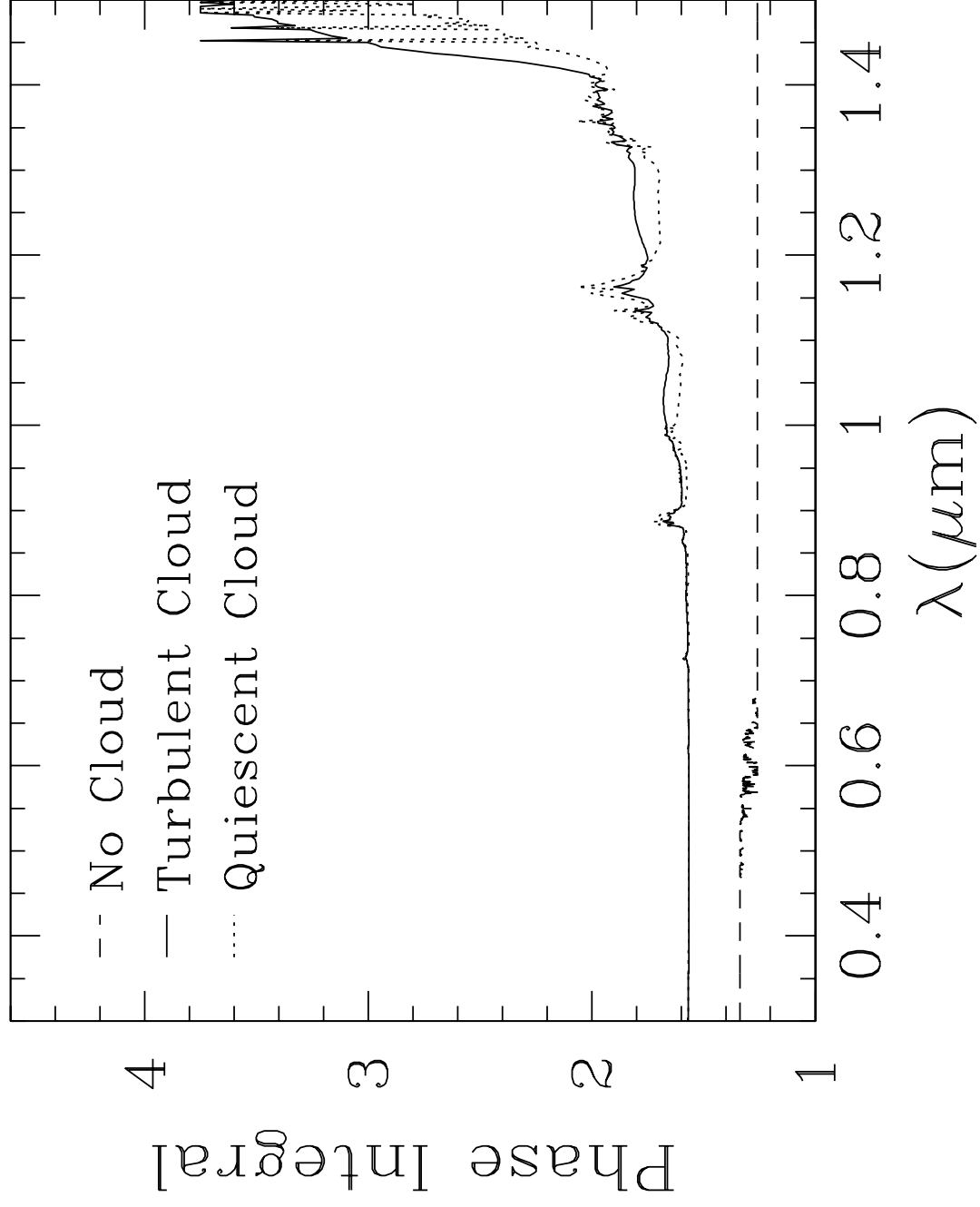


TABLE 1  
BOND ALBEDOS FOR CLOUD-FREE PLANETS

Gravity m/s <sup>2</sup>	$T_{\text{eff}}$ K	Mass <sup>1</sup> M <sub>J</sub>	A5V	F4V	F8V	Spectral Type G0V	G2V	G8V	K4V	M2V
5	128	0.8	0.43	0.42	0.37	0.37	0.35	0.29	0.23	0.09
	200	0.8	0.41	0.40	0.35	0.35	0.33	0.26	0.20	0.08
	250	0.9	0.41	0.39	0.34	0.34	0.32	0.26	0.20	0.07
10	200	1.3	0.41	0.39	0.34	0.34	0.32	0.25	0.19	0.07
	300	1.4	0.40	0.39	0.33	0.33	0.31	0.25	0.19	0.07
	500	1.6	0.42	0.40	0.35	0.35	0.33	0.26	0.20	0.07
22	128	2	0.42	0.41	0.35	0.35	0.33	0.27	0.21	0.08
	300	2	0.40	0.38	0.33	0.33	0.31	0.24	0.19	0.07
	1000	3	0.42	0.41	0.36	0.35	0.33	0.27	0.21	0.08
50	300	4	0.39	0.38	0.32	0.32	0.30	0.24	0.18	0.06
	400	4	0.40	0.38	0.33	0.32	0.30	0.24	0.18	0.06
	500	5	0.40	0.39	0.33	0.33	0.31	0.24	0.19	0.06
300	300	13	0.39	0.37	0.32	0.31	0.29	0.23	0.17	0.06
	1000	17	0.40	0.38	0.33	0.33	0.30	0.24	0.18	0.06
1000	250	26	0.40	0.39	0.33	0.33	0.31	0.25	0.19	0.06
	1000	36	0.40	0.39	0.33	0.33	0.31	0.24	0.19	0.06
3000	200	50	0.44	0.42	0.37	0.37	0.35	0.28	0.22	0.08
	1000	73	0.42	0.41	0.36	0.35	0.33	0.27	0.21	0.07

<sup>1</sup>Approximate mass given by  $M=36M_J(g/1000)^{0.64}(T_{\text{eff}}/1000)^{0.23}$ , where  $g$  is in m/s<sup>2</sup> and  $T_{\text{eff}}$  is in K (Marley, *et al.* 1996).



# Reflected Spectra and Albedos of Extrasolar Giant Planets I: Clear and Cloudy Atmospheres

Mark S. Marley, Christopher Gelino, Denise Stephens  
New Mexico State University

Jonathan I. Lunine  
Lunar and Planetary Laboratory, University of Arizona and Reparto di Planetologia, Istituto di  
Astrofisica, Rome, Italy

Richard Freedman  
Space Physics Research Institute, NASA/Ames Research Center

## ABSTRACT

The reflected spectra of extrasolar giant planets are primarily influenced by Rayleigh scattering, molecular absorption, and atmospheric condensates. We present model geometric albedo and phase integral spectra and Bond albedos for planets and brown dwarfs with masses between 0.8 and 70 Jupiter masses. Rayleigh scattering predominates in the blue while molecular absorption removes most red and infrared photons. Thus cloud-free atmospheres, found on giant planets with effective temperatures exceeding about 400 K, are quite dark in reflected light beyond  $0.6\ \mu\text{m}$ . In cooler atmospheres first water clouds and then other condensates provide a bright reflecting layer. Only planets with cloudy atmospheres will be detectable in reflected light beyond  $1\ \mu\text{m}$ . Thermal emission dominates the near-infrared for warm objects with clear atmospheres. However the presence of other condensates, not considered here, may brighten some planets in reflected near-infrared light and darken them in the blue and UV. Bond albedos, the ratio of the total reflected to incident power, are sensitive to the spectral type of the primary. Most incident photons from early type stars will be Rayleigh scattered, while most incident photons from late type stars will be absorbed. The Bond albedo of a given planet thus may range from 0.4 to 0.05, depending on the primary type. Condensation of a water cloud may increase the Bond albedo of a planet by up to a factor of two. The spectra of cloudy planets are strongly influenced by poorly constrained cloud microphysical properties, particularly particle size and supersaturation. Both Bond and geometric albedos are comparatively less sensitive to variations in planet mass and effective temperature.

*Subject headings:* extrasolar planets, spectra

## 1. Introduction

The indirect detection of planets surrounding nearby stars (Mayor & Queloz 1995; Marcy & Butler 1996; Butler & Marcy 1996; Butler et al. 1997; Cochran et al. 1997) has spurred efforts to both understand the origin and evolution of these bodies and to directly detect them. Evolution models depend upon a computation of the deposition of incident radiation into the planetary atmospheres and calculations of planetary albedos. Detection efforts require estimates of the spectra of the extrasolar planets. We present here models of the reflected spectra and albedos of extrasolar planets to facilitate both the modeling of the evolution of these objects and ultimately their direct detection.

While it is currently not known if the new objects are terrestrial planets, jovian planets, or even brown dwarfs, we focus here on jovian planets and brown dwarfs. Our justification is largely drawn from planetary formation models (e.g. Pollack et al. 1996), the cosmic abundance of the elements, and our prejudice from our own solar system, supported by minimum masses for the new objects exceeding  $0.4 M_J$ , where  $M_J$  is one Jupiter mass. Regardless of mass, we refer to these objects as Extrasolar Giant Planets (EGPs).

Saumon et al. (1996) presented the first comprehensive study of the evolution and spectra of extrasolar giant planets. They modeled the reflected component of the spectra as a graybody reflecting incident blackbody radiation. As Saumon et al. recognized, this approach overestimates the reflected flux from Jupiter by up to two orders of magnitude in certain bands. Thus a complete, non-gray, model of atmospheric scattering is required to fully model the reflected component of these atmospheres.

Burrows et al. (1997) reported on the evolution and emitted spectra of extrasolar jovian planets and brown dwarfs. They modeled solar composition objects and included the influence of neither incident sunlight nor clouds. Their thermal emission spectra extended from slightly shortwards of  $1 \mu\text{m}$  to beyond  $100 \mu\text{m}$ . To construct boundary conditions for their evolution models and emergent spectra, they computed radiative-convective equilibrium atmosphere models for over 50 objects with effective temperatures ranging from 128 to 1200 K and gravities between 22 and  $3000 \text{ m sec}^{-2}$ . This phase space covers the range from Jupiter to the most massive brown dwarfs. Burrows et al. found that the emergent flux from such objects can deviate strikingly from a blackbody, with fluxes in some bands orders of magnitude larger than those of a blackbody with the same effective temperature.

Here we report on the reflected spectra and albedos of extrasolar planets and brown dwarfs. To present as general a set of results as possible, we calculate the geometric albedo spectrum of each model planet. The actual reflected spectrum for a planet around an arbitrary star can be computed from the geometric albedo spectrum, the appropriate incident stellar spectrum, and the phase function of scatterers in the planetary atmosphere. The geometric albedo spectrum of Jupiter and Uranus in the optical are shown in Figure 1.

Condensates dramatically influence the reflected spectra of all the substantial atmospheres of our solar system. We explore the role of both silicate and water clouds in the reflected spectra of the extrasolar planets and brown dwarfs and discuss potential tests for clouds. However we postpone a detailed investigation of the role of condensates to a future paper.

We stress that we are not attempting to exactly predict the spectrum of a particular extrasolar planet. No observed reflected spectra yet exist for the extrasolar planets and their masses, compositions, and ages (and thus internal heat flows) are constrained poorly, if at all. Given the large uncertainties in atmospheric composition, atmospheric hazes, cloud decks, particle sizes and compositions, not to mention the poor quality of the high temperature absorption coefficients of many molecules of interest, we choose to examine the overall phase space of gravity and effective temperature within which the new planets reside. This work, in combination with Burrows et al. (1997), provides the means to quickly estimate the reflected and emitted flux from an extrasolar giant planet or brown dwarf. Detailed modeling of specific planets is retained for the future although Guillot et al. (1997a) have presented some of our early results for specific planets.

## 2. Albedo Computation

### 2.1. Theory

The Bond or bolometric albedo  $A$  is the ratio of the total power reflected by a planet to the total power incident upon the planet,

$$A = \frac{P_{\text{refl}}}{P_{\text{incid}}}. \quad (1)$$

This albedo is used to compute the planetary energy balance: the effective temperature  $T_{\text{eff}}$  at which a planet radiates to space is given by

$$4\pi R^2 \sigma T_{\text{eff}}^4 = E_{\text{int}} + \pi R^2 (1 - A) \pi S / d^2. \quad (2)$$

Here  $R$  is the radius of the planet,  $d$  is the distance to the sun in astronomical units,  $\pi S$  is the solar constant or flux at 1 AU,  $\sigma$  the Stefan-Boltzmann constant, and  $E_{\text{int}}$  represents the internal energy sources (e.g. Conrath et al. 1989). The total reflected flux  $\mathcal{F}_\nu$  received from an extrasolar giant planet a distance  $a$  from Earth that orbits a star of radius  $R_*$  is given by (e.g., Saumon et al. 1996)

$$\mathcal{F}_\nu = \frac{A}{4} P(\Phi) \left( \frac{R_*}{d} \right)^2 \left( \frac{R}{a} \right)^2 \mathcal{F}_\nu^*. \quad (3)$$

$\mathcal{F}_\nu^*$  is the flux radiated by the surface of the star and  $P(\Phi)$  is a function with value of order unity that accounts for the dependence of the reflected light upon phase angle  $\Phi$ , the angle between the star, the planet, and the observer.

To compute the Bond albedo, expressions are required for  $P_{\text{refl}}$  and  $P_{\text{incid}}$ . The incident power

is straightforward,

$$P_{\text{incid}} = \pi R^2 \frac{\pi S}{d^2}. \quad (4)$$

Neglecting any possible dependence of reflectivity on latitude (e.g. polar caps), the total reflected flux can be computed from the mean disk intensity  $\bar{I}(\Phi)$  by an integral over phase angle (Hanel et al. 1992),

$$P_{\text{refl}} = 2\pi^2 R^2 \int_0^\pi \bar{I}(\Phi) \sin \Phi d\Phi. \quad (5)$$

After the division of Eq. (5) by Eq. (4) it is possible to write

$$A = pq = \frac{\bar{I}(0)}{S/d^2} \cdot 2 \int_0^\pi \frac{\bar{I}(\Phi)}{\bar{I}(0)} \sin \Phi d\Phi. \quad (6)$$

This equation defines the second commonly used albedo, the geometric albedo  $p$

$$p = \frac{\bar{I}(0)}{S/d^2}. \quad (7)$$

The geometric albedo is simply the reflectivity of a planet measured at opposition. It can be expressed as either a mean value integrated over the solar spectrum,  $\bar{p}$ , or as a monochromatic value,  $p_\lambda$ . Spectra of Jovian planets are commonly presented as the latter. For a perfectly-reflecting Lambert sphere the geometric albedo is 2/3 (Hanel et al. 1992); for a semi-infinite purely Rayleigh scattering atmosphere it is 0.75 (Dlugach and Yanovitskij 1974).

The Bond albedo is then formally related to the monochromatic geometric albedo (e.g. Pollack et al. 1986) by

$$A = \int_0^\infty p_\lambda q_\lambda f_\lambda d\lambda \bigg/ \int_0^\infty f_\lambda d\lambda \quad (8)$$

where  $q_\lambda$  is the monochromatic phase integral and  $f_\lambda$  is the incident monochromatic solar flux. Following Eq. (6), the phase integral is defined by

$$q = 2 \int_0^\pi \frac{\bar{I}(\Phi)}{\bar{I}(0)} \sin \Phi d\Phi. \quad (9)$$

The phase integrals for a Lambert sphere and a Rayleigh atmosphere are 3/2 and 4/3 respectively.

While  $q_\lambda$  can vary with wavelength in a complicated manner, it is common to remove an appropriately averaged mean phase integral  $\bar{q}$  from the integral and let

$$A = \bar{q} \int_0^\infty p_\lambda f_\lambda d\lambda \bigg/ \int_0^\infty f_\lambda d\lambda \equiv \bar{q}\bar{p}. \quad (10)$$

With this approach the task of computing the Bond albedo falls to separately computing the mean phase integral and mean geometric albedo. Pollack et al. (1986), for example, computed  $\bar{p}$  and  $\bar{q}$  for a wide range of possible pre-Voyager Uranus atmosphere models, including models with strongly forward-scattering clouds and with isotropically-scattering clouds. They found that

$\bar{q}$  varied only by about  $\pm 10\%$  among different models, with a typical value of about 1.2. This is because most reflected photons near the peak of the solar Planck function are scattered by Rayleigh scattering, and the phase integral for Rayleigh scattering with a moderate amount of molecular absorption ranges between 1.25 and 1.30.

Unlike Pollack et al., after finding both  $q_\lambda$  and  $p_\lambda$  as a function of wavelength we compute  $A$  via Eq. (8) rather than Eq. (10). By varying  $f_\lambda$ , we compute Bond albedos for a variety of stellar types along the main sequence in Section 4.2.

## 2.2. Atmosphere Models

To compute the spectra for an atmosphere with a given effective temperature and gravity requires a model which describes an atmosphere with those characteristics. The most accurate way to proceed would be to compute a self-consistent radiative-convective equilibrium model atmosphere for each possible type of primary star, internal heat flow, orbital distance, and surface gravity. Such a model would compute both the deposition of incident radiation with height and the transport of internal energy. If the computed temperature profile crossed condensation equilibria contours, clouds would be inserted and the deposition of solar radiation recomputed. Indeed this approach was taken by Marley and McKay (1998) to compute atmospheric temperature profiles for Uranus and by Marley (1998) for exploratory models of EGP atmospheres.

However, given the large phase space of models which we wish to explore, we choose not to compute atmosphere models which include the deposition of solar radiation. Rather we use the temperature profiles presented in Burrows et al. (1997) which are computed for isolated brown dwarfs and extrasolar planets. In addition, several new, lower gravity models (down to  $g = 5 \text{ m sec}^{-2}$ ) were also computed for this work, following the techniques presented in Burrows et al. (1997).

We then ask what these models would look like under various illumination conditions. In other words, we compute the reflected spectra of “isolated” brown dwarfs and extrasolar planets. In doing so, we neglect the effect of the incident radiation on the temperature profile. Incident radiation would have two main effects on the models. Firstly, methane would absorb incident radiation above the tropopause, producing a warm stratosphere as in the solar Jovian atmospheres. This behavior is seen in exploratory extrasolar atmosphere models (Marley 1998). Except for those few objects where the tropopause temperature may rise sufficiently to prevent condensation, for most objects with a fixed effective temperature, the change in the temperature profile resulting from absorption of the direct insolation should not substantially alter the reflected spectra calculated here. Secondly, incident UV radiation will drive photochemical reactions that can produce stratospheric hazes. As discussed in Section 3.4 such hazes will both absorb additional incident UV radiation and scatter infrared photons thereby affecting both the temperature profile and the reflected spectrum. Results from a detailed investigation will be presented in a future



paper.

Each atmosphere model consists of up to 53 levels, spaced approximately evenly in the log of atmospheric pressure. In each layer (layers describe the atmosphere between discrete levels) the single scattering albedo  $\tilde{\omega}_0$  and scattering asymmetry factor are computed for the relevant scatterers. Mean values of these parameters are found for each layer by weighting each constituent’s scattering parameters by its layer scattering optical depth. Opacity sources are discussed in the next section.

The geometric albedo spectra are then computed following the approach employed by McKay et al. (1989). The source function from the Eddington two-stream approximation is used in an exact integral of the radiative transfer equation. This Eddington source function technique and the associated errors are described in Toon et al. (1989). The ratio of emergent to incident intensities are integrated over the disk to compute the geometric albedo as a function of wavelength. Previous applications of this code have reproduced the geometric albedo spectrum of Titan and Uranus (McKay et al. 1989; Marley and McKay 1998).

For some models, particularly the warm, high gravity models, optical depth unity at some wavelengths near  $0.4$  to  $0.5\,\mu\text{m}$  is not reached above the bottom of the model atmosphere. This is because the column number density of absorbers and scatterers is low for such models. For these models we extend the bottom of the model to 1,000 bars by extrapolating the temperature along an adiabat. Any remaining downward propagating photons at this level are assumed lost.

The phase integral is a function of the scattering properties of the atmosphere. For a conservative Rayleigh atmosphere  $p = 1.33$ . As the single scattering albedo falls, multiple scattering becomes less significant, the geometric albedo decreases, and  $q$  decreases. Dlugach and Yanovitskij (1974) present tables of  $q_\lambda$  as a function of  $\tilde{\omega}_0$  for purely Rayleigh scattering atmospheres. We compute the monochromatic phase integral for the clear atmospheres by interpolation within these tables. For a purely Rayleigh atmosphere the phase integral is not highly sensitive to  $\tilde{\omega}_0$ . Over the tabulated range of  $\tilde{\omega}_0$ ,  $p_\lambda$  varies from 0.75 to 0.2, while  $q_\lambda$  varies only between 1.33 and 1.26. For cases of small  $\tilde{\omega}_0$  that fall outside the tables, we set  $q = 1.25$ . Since the low values of  $\tilde{\omega}_0$  are found in the infrared where  $f_\lambda$  is also comparatively small, the exact treatment of  $q$  for small  $p$  has no influence on the Bond albedo.

Since the scattering phase function of cloudy planets differs from a Rayleigh phase function, we compute  $q$  for the cloudy cases by interpolating within tables of Dlugach and Yanovitskij (1974) that give  $q$  as a function of both  $\tilde{\omega}_0$  and the scattering asymmetry parameter. In these cases the scattering behavior depends on whether or not the clouds are visible at a given wavelength. For wavelengths in which the normal scattering optical depth reaches unity above the cloud layer, we proceed as above for a purely Rayleigh atmosphere since the clouds are not visible. When most photons are scattered in the cloud, we compute the mean layer asymmetry factor and single scattering albedo at that wavelength for the layer in which the normal scattering optical depth reaches unity. We then interpolate to find  $q_\lambda$ . Some sample  $q_\lambda$  spectra are shown in Figure 2.

Since  $q_\lambda$  varies only weakly between models, we do not present multiple plots of this parameter.

Our approach for a purely Rayleigh scattering, absorbing atmosphere is near exact. For the three cloudy atmospheres we consider here, the computed values of  $q_\lambda$  are estimated to be accurate within 10%. In a future paper we will consider a broader range of cloud models and present an exact calculation of  $q_\lambda$ .

### 3. Atmospheric Opacity Sources

The atmosphere models presented in Burrows et al. (1997) assumed solar elemental composition. Chemical equilibrium abundances for all species are computed for each model layer and a self-consistent radiative-convective equilibrium temperature profile is derived. For these same models we compute the reflected radiation. In this section we summarize the major contributors to atmospheric opacity at wavelengths shorter than  $5\mu\text{m}$ .

#### 3.1. Rayleigh Scattering

For a semi-infinite, purely molecular atmosphere, all photons received by an observer have been returned by Rayleigh scattering. A rigorous treatment of Rayleigh scattering would employ the full phase matrices to compute the intensity of scattered light. Indeed Pollack et al. (1986) investigated the difference in computed geometric albedos for calculations which employed the full phase matrix and those which simply used a scalar phase function. They found that in an infinitely-deep purely Rayleigh atmosphere the scalar phase function treatment of Rayleigh scattering resulted in an under-estimate of the geometric albedo by about 6%.

Pollack et al. employed an empirical correction scheme to account for this discrepancy. We choose instead to normalize our treatment of the Rayleigh phase integral so that our code returns the correct geometric albedo (0.75) in the limit of an infinitely-deep purely Rayleigh atmosphere.

#### 3.2. Raman Scattering

Belton et al. (1971) first recognized the importance of Raman scattering in decreasing the ultraviolet geometric albedo in deep, Rayleigh scattering planetary atmospheres. During Rayleigh scattering a fraction of photons excite vibrational and rotational transitions of  $\text{H}_2$ . The scattered photons thus experience a shift to longer wavelengths. Excitation of rotational transitions produces very small wavelength shifts and is responsible for “Raman ghosts” of solar Fraunhofer lines. We are concerned instead with the much larger shifts arising from excitation of vibrational transitions, which removes photons from the UV and blue.

Pollack et al. (1986) discuss several approximate and exact techniques for computing the effect of Raman scattering on the geometric albedo spectrum. They find that in a deep  $\text{H}_2$  atmosphere Raman scattering can decrease the geometric albedo by 20% at  $0.3\,\mu\text{m}$ . We choose the same approximation for Raman scattering as adopted by Pollack et al. and express the mean single scattering albedo  $\tilde{\omega}_0$  of a layer as

$$\tilde{\omega}_0 = \frac{\sigma_{\text{R}} + \sigma'_{\text{S}} + \sigma_{\text{RA}}(f_{\lambda^*}/f_{\lambda})}{\sigma_{\text{R}} + \sigma'_{\text{e}} + \sigma_{\text{RA}}}. \quad (11)$$

Here  $\sigma$  denotes the cross sections for Rayleigh scattering (subscript R), Raman scattering (RA), scatterers other than  $\text{H}_2$  (S), and other sources of extinction (e). The ratio  $f_{\lambda^*}/f_{\lambda}$  accounts for the wavelength dependence of the incident solar spectra. The wavelength of interest is denoted by  $\lambda$  and  $\lambda^{*(-1)} = \lambda^{-1} + \Delta\lambda^{-1}$ , where  $\Delta\lambda$  is the wavelength of the  $\text{H}_2$  vibrational fundamental  $\Delta\lambda^{-1} = 4161\,\text{cm}^{-1}$ . The Raman correction is confined to wavelengths less than the peak of the Planck function, thus limiting the maximum single scattering albedo to be less than 1. Pollack et al. (1986) find that geometric albedos computed with this approximation match well those computed with an exact treatment of Raman scattering.

The geometric albedo spectra presented in Section 4 are computed using values of  $f_{\lambda^*}/f_{\lambda}$  computed for a 6000 K blackbody, an adequate approximation since we are most interested in the general shape of the spectrum. For a rigorous calculation of the spectra of a particular planet, the flux ratio appropriate to the particular primary must be used. Over the range of spectral types considered here, this approximation changes  $p_{\lambda}$  by only a few percent at the shortest wavelengths. For very early type stars (O and B) the stellar Planck function peaks in the ultraviolet and Raman scattering would have the opposite sign in the UV, but such models are not considered here.

### 3.3. Molecular Opacities

The sources of molecular opacity data and the treatment of line broadening is discussed fully in Burrows et al. (1997). Our approach differs only in that we do not treat opacities with the k-coefficient technique, but rather compute exact fluxes on a fixed wavelength grid. The opacity within a given atmospheric layer is a function of its composition, temperature, and pressure. We interpolate within opacity tables computed for fixed conditions within the model to find the opacity of a given species at arbitrary temperature and pressure.

In the spectral region considered here, the most important molecular opacities are those of water, ammonia, methane, and pressure-induced absorption by hydrogen. Ammonia bands lie near  $0.64$  and  $0.78\,\mu\text{m}$  and between  $1.4$  and  $1.55\,\mu\text{m}$ ,  $1.9$  and  $2.05\,\mu\text{m}$ , and  $2.2$  and  $2.4\,\mu\text{m}$ . The major methane absorption bands lie at  $0.725$ ,  $0.89$ ,  $1.0$ ,  $1.15$ ,  $1.4$ ,  $1.7$ , and  $2.5\,\mu\text{m}$  with many other weaker bands in the optical. Water bands are important for the warmer objects considered here. The strongest bands in the optical lie at  $0.83$  and  $0.95\,\mu\text{m}$ . Stronger bands fall at  $1.1$ ,  $1.4$ ,  $1.9$ , and  $2.9\,\mu\text{m}$ . The fundamental of the pressure-induced vibrational band of molecular hydrogen is

centered at  $2.4\,\mu\text{m}$  and the first overtone is at  $1.2\,\mu\text{m}$ . Several other weaker hydrogen features populate the visible.

### 3.4. Photochemical Hazes

As is apparent for Jupiter and Uranus in Figure 1, the geometric albedo in the UV and blue for all the solar Jovian planets is lower than predicted for purely Rayleigh (and Raman) scattering atmospheres (e.g. Savage and Caldwell 1974). Hazes created by the photochemical destruction of methane and other molecules produce a smog of particles that are dark in the blue and ultraviolet. There is a rich literature of observations and models of such hazes in planetary atmospheres. Indeed these hazes were first recognized from the depressed UV and blue geometric albedos of the planets. Furthermore the photochemical products themselves (e.g.  $\text{C}_2\text{H}_2$  and  $\text{C}_2\text{H}_6$ ) also absorb in the ultraviolet.

While the presence of the hazes is known and their origin well understood, they are particularly difficult to model. Their size and vertical distribution depends on photochemical reaction rates, eddy mixing coefficients, and nucleation and coagulation rates that are poorly known. In warm extrasolar atmospheres rich in C, N, O, and S bearing molecules, it is likely that photochemistry will yield a particularly complex brew of non-equilibrium compounds (Marley 1998). Both the compounds themselves and any resulting condensates may lower the reflected UV flux. Indeed even recent attempts to model the hazes detected by Voyager have met with only partial success (e.g. Rages et al. 1991, Moses et al. 1995). Thus we neglect photochemistry in our model atmospheres while recognizing that its influence may be significant. Photochemical hazes would likely depress the geometric albedo in the blue and UV while increasing the albedo in the near-infrared molecular bands of water and methane (by scattering photons before they are absorbed). As a result the Bond albedos for planets orbiting early type stars will be quite sensitive to the effects of photochemistry.

### 3.5. Clouds

We also consider the role of clouds in affecting planetary reflected spectra. A cursory look at any of the planets in our solar system with a substantial atmosphere, including Earth, reveals that clouds dramatically affect the visible appearance of planets. Guillot et al. (1997b) have explored condensation processes in the atmosphere of extrasolar giant planets. They find that at effective temperatures above about 1100K silicates, including  $\text{MgSiO}_3$ , condense in the atmosphere. At effective temperatures below about 400 K, water condenses. At intermediate temperatures lower abundance species, such as  $\text{Na}_2\text{S}$  and  $\text{ZnS}$  condense. At the very cool temperatures characterizing the atmospheres of our own jovian planets  $\text{NH}_4\text{SH}$ ,  $\text{NH}_3$ , and  $\text{CH}_4$  also condense. Thus all of the atmospheres considered in this paper likely contain hazes or clouds of various species. There is no

doubt that these condensates will alter the reflected spectra of extrasolar giant planets. To explore the potential effects of these condensates we will concentrate on the most abundant condensates, water and enstatite,  $\text{MgSiO}_3$ .

In this section we discuss models for the physical size and vertical extent of water and silicate clouds and consider their effect on the atmospheric opacity.

### 3.5.1. *Cloud Profiles*

The characterization of the physical properties and radiative effects of condensed species in an atmosphere is a difficult exercise unless extensive observations are available. Experience with the Earth shows that cloud particle sizes, vertical and horizontal distributions are sensitive functions of the ambient atmospheric conditions. In the terrestrial atmosphere a strong feedback exists between cloud evolution and the background temperature, winds and vertical turbulent motions. On the other hand, the simplest model in which the vapor pressure relationship of the condensed species is used to predict cloud properties is inadequate because no information on condensate particle size is available from this equation by itself.

Ultimately detailed fitting of high-resolution spectra will enable extraction of information on the globally-averaged cloud properties of extrasolar planets and brown dwarfs. As a start to this process, we have constructed a simple scheme to predict the particle size as a function of altitude for two condensible species, water and magnesium silicate, in two end-member environments corresponding to quiescent and turbulent atmospheric states. The model builds on an earlier scheme in Lunine et al. (1989). We begin with the cloud-free atmospheric models whose construction is described above, and use the temperature-pressure profile (along with assumption of roughly local solar elemental abundance) to determine the cloud base and vapor abundance as a function of altitude. Vapor pressure relations for water (liquid and solid) are from Eisenberg and Kauzmann (1969), for solid magnesium silicate from Barshay and Lewis (1976).

Given the vapor pressure abundance we compute a maximum mixing ratio of condensate in the cloud-forming region by taking the vapor abundance and multiplying by a suitable supersaturation factor, which yields the amount of condensible available for condensation. The supersaturation is formally defined as  $f_s = (P_v/P_s) - 1$ , where  $P_v$  is the actual vapor pressure reached prior to condensation and  $P_s$  is the thermodynamic saturation vapor pressure of water or silicates over the same type of condensate (ie., solid or liquid). The supersaturation varies widely among and within planetary atmospheres, and is a sensitive function of the local properties of condensation nuclei which are not well known for extrasolar planets; generally the supersaturation for a given condensable species is larger in colder atmospheres and in the relative absence of nucleating aerosols. As a baseline we choose  $f_s = 0.01$ , so that the condensate abundance at each atmospheric altitude is 1% the vapor phase abundance. This number is simply a typical value which fits some terrestrial situations involving condensation onto nucleating sites, but needs to be recomputed in

actual fitting of high resolution observational spectra to results of spectral synthesis models (see, for example the Courtin et al. (1995) analysis for Titan). For the given supersaturation factor we regard our condensate abundances as practical upper limits because physical processes such as sedimentation, atmospheric downwelling, etc., will tend to decrease the globally-averaged column abundance of cloud particles. However to evaluate the sensitivity of the computed spectra to this parameter, we also consider cases with other values of  $f_s$ .

To estimate the cloud particle size we follow one of two approaches. In the first, we employ a simple model to compute the variation of cloud particle size with height in quiescent and turbulent atmospheres. In the second we explore the spectral sensitivity to changes in particle size by considering a suite of particle sizes independent of any condensation model.

For the first approach, we employ the formalism of Rossow (1978) who computed timescales associated with grain growth by condensation and agglomeration, and loss by sedimentation. The equations for the various growth and loss processes are given in Rossow (1978) and will not be reproduced here. We further consider two endmember atmospheric situations. A *quiescent* atmosphere is one in which turbulence does not generate macroscopic eddy motions which serve to keep relatively large particles from rapidly sedimenting out of the cloud layer. In the quiescent atmosphere we balance, as a function of particle size, the growth rate (by condensation or coagulation, whichever is faster), against the sedimentation rate. Particles large enough such that the sedimentation rate just exceeds the growth rate are assumed to be the modal particle size. Since we do this at each level within the cloud we get a profile of cloud particle size and cloud particle density throughout the cloud. For the *turbulent* atmosphere the same procedure is followed, but here we compute the rate of eddy mixing and balance it against the sedimentation rate as a function of particle size. Particles large enough that the sedimentation rate just exceeds the rate of remixing by eddy turbulence are again assumed to fall out of the cloud. The eddy mixing rate is  $[(\mathcal{R}\sigma T_{\text{eff}}^4)/(\rho\bar{\mu}c_p)]^{1/3}(3H)^{-1}$ , where  $H$  is scale height,  $\mathcal{R}$  the gas constant,  $\bar{\mu}$  the atmosphere’s mean molecular weight,  $\rho$  its density and  $c_p$  its specific heat.

The radiative-convective atmosphere models describe which regions of the atmosphere are convective and which are radiative, thus presumably predicting whether the turbulent or quiescent cloud model is most applicable to a given situation. However, these calculations are made for a clear atmosphere. The presence of the cloud layers themselves will change the predicted profile, so we consider grain growth in both environments.

The resulting particle sizes as a function of altitude for the turbulent case are significantly larger than for the quiescent atmosphere, in agreement with terrestrial observations. Figures 3a and b illustrate the physical properties of the cloud models. For a typical model designed to approximate the brown dwarf Gℓ 229 B, with effective temperature of 1000 K and roughly 40 Jupiter masses, enstatite ( $\text{MgSiO}_3$ ) clouds have their base at 48 bars. In the quiescent case maximum particle sizes near the base are 30 microns at the base dropping to 2 microns higher in the cloud. In the turbulent case particle radii have a very narrow maximum size range throughout

the cloud of between 100 and 300 microns.

To better elucidate the dependence of the computed spectra on particle size, we also explore clouds of various uniform, fixed, sizes. Atmospheric condensates found in the solar system range from submicron photochemical hazes to micron-sized methane clouds (Rages et al. 1991), to even larger drops. Indeed the upper particle size limit for even Jupiter’s clouds is not well constrained. We thus consider clouds with fixed radii varying from 0.1 to 100  $\mu\text{m}$ .

### 3.5.2. *Mie Scattering*

The radiative effects of clouds were modeled by Mie scattering theory. The extinction and scattering efficiencies, single scattering albedos, and scattering asymmetry parameters were computed for spherical drops of water and enstatite. Mie scattering computations for drops of a single particle size show numerous, very high frequency, spectral features resulting from constructive and destructive interference of radiation inside and around an idealized drop. Since real clouds are composed of drops of a range of sizes, such fine structure becomes washed out and is seldom observed. We thus assume that the model clouds are characterized by a log-normal size distribution with a width parameter of 1.5. This size distribution is motivated by observations of real clouds in a variety of planetary atmospheres (e.g. Venus, Titan, and Uranus) and was chosen because the high frequency spectral features are removed while preserving the most physically significant variations in particle scattering parameters with wavelength. Detailed models of cloud particle nucleation, evaporation, sedimentation, and coagulation can motivate particular choices for the width parameter, but until such studies are motivated by exceptionally detailed spectra of extrasolar planets, such concerns are as yet premature. Other choices for the particle size distribution function are likewise possible, but all choices are currently equally unmotivated at this time by data or theory.

More complex treatments of scattering by condensates are possible. For example rhomboid or even fractal particles can be considered. The influence of such non-spherical particles primarily is apparent in the scattering asymmetry. However such treatments are usually only justified when the radiative transfer problem is exceptionally well constrained, generally uncertainties in Mie scattering are far less than the other unconstrained aspects of the problem. As the cloud particle sizes and shapes are essentially unconstrained, going beyond Mie theory is unwarranted.

The choice of composition and particle size determines the Mie scattering parameters. For water we use the optical properties of Hudgins et al. (1993). For the silicate clouds we employed the optical properties of amorphous enstatite from Scott and Duley (1996). The extinction optical depth of a model layer is then given by

$$\tau = \pi r_c^2 Q_{\text{ext}} \mathcal{N} \quad (10)$$

where  $r_c$  is the mean layer cloud particle size,  $\mathcal{N}$  is the layer column number density, and  $Q_{\text{ext}}$  is

the Mie extinction efficiency for the given particle composition and size. Scattering and absorption optical depths are similarly computed. Mie theory predicts that the extinction efficiency at optical wavelengths will be essentially constant for all particles with  $r_c > 1 \mu\text{m}$ . Since the total condensible mass in the atmosphere is fixed for a given model,  $\mathcal{N} \propto r_c^{-3}$  and  $\tau \propto r_c^{-1}$  for  $r_c > 1 \mu\text{m}$ .

### 3.6. Stellar Spectra

Fourteen stellar spectra (spectral type A5V-M6V) were taken from the Bruzual-Persson-Gunn-Stryker Spectrophotometry Atlas (Space Telescope Science Institute Data Analysis System; Gunn and Stryker 1983; Strecker et al. 1979). Spectra from the atlas are normalized to V magnitude 0. We renormalized each spectra by multiplying the spectral flux  $f_\lambda$  by the ratio of  $\sigma T_{\text{eff},*}^4$  to the integrated atlas flux, where  $T_{\text{eff},*}$  is the stellar effective temperature. Stellar fluxes were extended beyond  $2.56 \mu\text{m}$ , the limit of the atlas, with a Planck function of the same effective temperature. The integrated albedos are not sensitive to the details of the flux at these wavelengths.

Reflected fluxes are computed for a planet 1 AU from its primary star with radius from the table in Lang (1992). Planetary radii for each model were derived from scaling relations in Marley et al. (1996). Spectra are computed by multiplying the incident stellar flux by the geometric albedo. For objects observed at arbitrary phase, these spectra must be modified to account for the partial illumination of the disk and the phase function of atmospheric scatterers. For an object at half phase ( $\Phi = 90^\circ$ ) the total correction factor would be near 0.6.

## 4. Model Results

### 4.1. Geometric Albedo Spectra

#### 4.1.1. Planetary Spectra

Before discussing model results, we first compare the predictions of our model to the known Jovian planet spectra. Figure 1 displays the geometric albedo spectrum of both a cloud-free and a cloudy model with Jupiter’s gravity and effective temperature. Also shown are the geometric albedo spectra of Jupiter and Uranus. All these spectra are dominated by the optical bands of methane. However the clear model spectrum appears more similar to the spectrum of Uranus than that of Jupiter. This is because Uranus’ visible atmosphere is clearer, deeper, and contains 10 times more methane (Lindal 1987) than Jupiter’s. These characteristics, coupled with the planet’s lower gravity, result in a 40-fold larger column abundance of  $\text{CH}_4$  above the uppermost cloud deck than in Jupiter’s atmosphere. Since the clear model does not have a lower reflecting boundary, the model appears more similar to Uranus than to Jupiter. The cloudy model, with its high aerosol haze and thick cloud is meant to only roughly represent Jupiter. An exact fit requires the fine



tuning of far more model parameters than we explore here.

Scattering from bright clouds also accounts for the brightness of both Jupiter and Uranus in-between methane absorption bands beyond  $0.6\,\mu\text{m}$ . In Jupiter’s atmosphere upper cloud decks of  $\text{NH}_3$  and  $\text{NH}_4\text{SH}$  scatter incident radiation back to space before it can be absorbed. In the perfectly clear model atmosphere downward photons in the red and beyond are lost to weak molecular absorption long before they can Rayleigh scatter back to space. Thus the clear model is almost black beyond  $1\,\mu\text{m}$  while Jupiter, Uranus, and the cloudy model remain bright between the strong  $\text{CH}_4$  and  $\text{H}_2 - \text{H}_2$  bands which define the near-infrared spectra. Indeed, were it not for its clouds and hazes, Jupiter would be essentially undetectable in reflected light in the near infrared.

At wavelengths less than about  $0.65\,\mu\text{m}$  Jupiter is darker than the model. As discussed in Section 3.4, this difference is attributable to the presence of absorbing hazes high in Jupiter’s stratosphere. These hazes lower the mean single scattering albedo of the atmosphere below that expected for a purely Rayleigh and Raman scattering atmosphere. Some thin UV-dark hazes also somewhat depress the UV albedo in Uranus’ atmosphere. Again, however, the clear, Rayleigh and Raman scattering model atmosphere is more similar to Uranus than to Jupiter. Jupiter’s albedo is also lowered in this wavelength region by absorption by other hydrocarbons. The bright cloudy model scatters some UV photons before they can be Raman scattered and is thus bright in the UV.

Finally, many of the high frequency features seen in both Jupiter’s and Uranus’ spectra are Raman ghosts, discussed in Section 3.2. These features do not appear in the model spectrum since we neglect Raman rotational scattering.

As the above comparisons suggest, only models optimized to fit an individual planet’s atmosphere can hope to exactly match the spectra of a given planet. The planetary spectra in Figure 1 can be reproduced exactly only by including multiple cloud and haze layers with wavelength dependent scattering properties (e.g. Baines and Bergstralh 1986). These quantities are determined by carefully fitting the observed spectra. There is no theory that *predicts* these quantities. Given these empirical difficulties, our approach is simply to explore the sensitivity of planetary albedo to various model parameters.

#### 4.1.2. *Cloud-free EGP Spectra*

Model geometric albedo spectra for clear and cloudy atmospheres are shown in Figures 4 through 7. In each case the spectra were computed for 3,300 points between  $0.3$  and  $5\,\mu\text{m}$  and then smoothed with a Gaussian to produce the figures.

The sensitivity of the cloud-free model spectra to gravity and effective temperature is explored in Figures 4 and 5. Figure 4 compares the spectra of three models with Jupiter’s effective temperature but differing gravity. These spectra all demonstrate that deep, cloud-free

atmospheres are remarkably dark in reflected light beyond about  $0.6\,\mu\text{m}$ . Among the models is very little sensitivity to changes in gravity. The main trend is that the reflectivity falls with increasing gravity. This and the other differences arise from the differing temperature profiles (different number densities at a fixed pressure), and relative differences in the strength of molecular absorption and Rayleigh scattering.

Figure 5 compares the geometric albedo of two cloud-free models with Jupiter’s gravity, but differing  $T_{\text{eff}}$ . These correspond to objects with masses of about 2 and 3  $M_{\text{J}}$ . Again there are relatively few differences in the two spectra. The principle differences are the appearance of an ammonia band at  $0.62\,\mu\text{m}$  and some differences in band depths. In the warmer atmosphere nitrogen is present as  $\text{N}_2$  and a pressure-induced  $\text{H}_2$  absorption feature near  $0.82\,\mu\text{m}$  is more prominent in the cooler, denser model since the absorption is proportional to the square of the number density. The presence of ammonia thus serves as a temperature discriminant. As temperatures drop further water condenses and the water bands becomes less prominent in the optical. In the near-infrared, however, where photons penetrate more deeply, water continues to be an important absorber.

As these results demonstrate, the cloud-free EGP spectra are relatively insensitive to changes in gravity and effective temperature. The main spectral indicators for objects cooler than about 1200 K are first the appearance of the relatively subtle  $\text{NH}_3$  bands, which start to appear for  $T_{\text{eff}} < 1000\text{ K}$  and the disappearance of the water bands below about 400 K. As discussed in the next section, clouds leave a far greater imprint on the spectra.

#### 4.1.3. Cloudy Spectra

The spectra presented in the previous section are limiting cases since real atmospheres will certainly have condensates. Guillot et al. (1997b) and Burrows and Sharp (1998) have investigated condensation in EGP atmospheres. They find that water condenses in the atmospheres of objects with  $T_{\text{eff}} < 400\text{ K}$ . Although there will be some condensates present in warmer atmospheres (section 4.1), the sudden appearance of bright water clouds will dramatically alter the reflected spectra of a planet cooling through 400 K. Silicate clouds will form in the observable portion of the atmosphere only for objects with effective temperatures above about 1000 K

The influence of water clouds is illustrated in Figures 6a, b, and c. The quiescent and turbulent (Fig 6a) spectra correspond to the cloud models shown in Figure 3a for a  $2M_{\text{J}}$ , 300 K planet. In Figure 6a the atmosphere is assumed to be highly supersaturated ( $f_s = 1$ ) to demonstrate the maximum influence of clouds. In this model the water clouds produce a dramatic increase in the reflected flux beyond about  $0.6\,\mu\text{m}$ . by providing a bright reflecting layer high the atmosphere that scatters red and near-infrared photons before they have a chance to be absorbed. Longwards of about  $1.5\,\mu\text{m}$  molecular absorption above the cloud tops is sufficiently strong to darken the planet despite the presence of the cloud. Since the cloud particle size increases with

depth into the cloud (from 2 to  $128\mu\text{m}$  at the cloud base for the radiative cloud), photons will scatter from the cloud at progressively deeper levels with increasing wavelength, providing greater opportunity for absorption before scattering. The difference between the two cloud models is a product both of the differing scattering properties of the differing particle size and, primarily, the differing particle number density attributable to the differing drop volume in the two models.

The importance of the supersaturation factor is demonstrated by Figure 6b. For each decade drop in  $f_s$  the cloud particle column number density and the cloud optical depth (Eq. 10) proportionately fall. Beyond  $1.5\mu\text{m}$  the residual cloudy albedo is still many orders of magnitude larger than that of the cloud free (Figure 4) atmosphere. In the optical the albedo is clearly sensitive to the supersaturation factor. For this case the  $f_s = 0.1$  and  $0.01$  models are almost identical to the cloud free model. This is not a general result as the total cloud column optical depth will vary with effective temperature, gravity, and cloud model. Nevertheless the strong sensitivity to the unknown  $f_s$  is unmistakable.

In Figure 6c the quiescent and turbulent clouds of Figure 3a have been replaced with various single particle sizes. Several factors are at work in the strong dependence of the spectra upon cloud particle size evident in this plot. For the smaller particle sizes there are many more drops, thus increasing the cloud optical depth and the albedo (see Section 3.5.2). The  $1\mu\text{m}$ -drops are most abundant of all and also are far more efficient Mie scatterers. Thus, like  $f_s$  the cloud particle size plays a decisive role in the planetary albedo.

Taken together, Figures 6a, b, and c demonstrate that any prediction of the importance of clouds in an EGP atmosphere must account for cloud microphysics, particle size, and supersaturation. Since all these quantities are completely unconstrained, only ranges of possible spectra can be predicted for an arbitrary planet.

The effects of silicate clouds on the reflected spectra of a brown dwarf are shown in Figures 7a, b, and c. In this case the silicates darken the brown dwarf in the visible and are less detectable in the infrared. Compared to the water cloud, the silicate cloud lies much deeper in the atmosphere (Figures 3a and b) and infrared photons do not penetrate deeply enough to sense the cloud. However in the visible some photons do multiply scatter to the depth of the the cloud deck. Since the silicate grains do not scatter conservatively, the geometric albedo is lower for the cloudy cases. The visibility of the silicate cloud also demonstrates the smaller scale height of the model atmosphere for the more massive object.

The large gravities of massive extrasolar giant planets and brown dwarfs often defy the intuition gained from studying the solar Jovian planets. Consider a cool brown dwarf similar to Jupiter, but more massive. It will have almost the same radius and thus a larger gravity. The large gravity means that to compress a parcel of the atmosphere to a given pressure, a smaller column number density of molecules is required. In other words, given identical pressure-temperature relations, the scale height for the atmosphere of the more massive planet is everywhere smaller. Thus given the same atmospheric composition, unity optical depth is reached at a larger pressure

in the more massive planet’s atmosphere. This is why it is possible to see the effects of a cloud which lies at 40 bars in a 36 M<sub>J</sub> object, but not in Jupiter’s atmosphere.

The effect of  $f_s$  on the quiescent cloud is demonstrated in Figure 7b. As with the water cloud the influence of the cloud depends sensitively on the total cloud optical depth and consequently  $f_s$ . The sensitivity to particle size is presented in Figure 7c. The submicron cloud both absorbs more efficiently at short wavelengths and scatters more efficiently in the infrared.

As these results demonstrate, in the near-infrared any scatterer, even ones with low  $\tilde{\omega}_0$  can substantially brighten the planet by reflecting incident light before it can be absorbed. The dark hydrocarbon hazes in the atmospheres of all four solar Jovian planets are well known examples. The impact scars left by the fragments of comet Shoemaker-Levy/9, which were dark at visible wavelengths and extraordinarily bright in the near-infrared, are other examples. The depth and shape of near-infrared absorption bands will thus provide a powerful constraint on the nature of clouds and aerosols in the extrasolar atmospheres.

## 4.2. Bond Albedos

Table I lists Bond albedos computed for a variety of cloud-free extrasolar giant planet model atmospheres and primary types. The masses of each object with a specified effective temperature and gravity are estimated using the approximate fitting relation given in Marley et al. (1996). This expression does not fit the lowest mass objects precisely (it predicts  $M = 2 M_J$  for Jupiter’s gravity and  $T_{\text{eff}}$ ), and so the masses should be viewed only as a guide. Bond albedos for the cloudy models are shown in Table 2. This table presents albedos for both  $f_s = 0.01$  and 0.1 as well as for all the cloud types discussed above.

Consistent with the spectra presented in Figures 4 and 5, the Bond albedos in Table 1 show very little sensitivity to gravity or effective temperature. For a given stellar primary the Bond albedo is constant to within about 10% for objects that vary by an order of magnitude in temperature and a factor of 100 in mass. This variation is comparable to or even smaller than the uncertainty in the Bond albedos for the solar Jovian planets (Conrath et al. 1989). The poorly constrained phase integral is most responsible for the large error bars for the Jovian planets.

The large range in possible cloud models translates to a very large range in Bond albedos in Table 2. Depending on the model, clouds can increase the Bond albedo by as much as a factor of 2. These variations are more clearly presented in Figures 8 and 9.

These figures show the possible variation in Bond albedo for Jupiter mass (Figure 8) and brown dwarf mass (Figure 9) objects. The general trend for all models is that the later the primary type, the lower the Bond albedo. The origin of this trend is immediately apparent from the geometric albedo spectra shown in the preceding section. Because of the decrease in the strength of Rayleigh scattering and the increase in the strength of molecular opacities, particularly

methane and water, with wavelength, extrasolar Jovian planets are darker in reflected light in the infrared than they are in the visible. The Bond albedo is defined, via Eq. (8) as a weighted average of  $p_\lambda q_\lambda$  over the incident flux. Since the Planck function of later type stars peaks at progressively longer wavelengths, the Bond albedo falls with the stellar type of the primary as one goes to later types along the main sequence.

These figures also demonstrate the great influence of clouds. The Bond albedo can vary by a factor of two for a fixed primary type when clouds are added to the atmosphere. As with the geometric albedo, the large sensitivity to cloud type arises from a combination of differing scattering properties and different column number densities for the various cloud models.

## 5. Discussion

The spectra of extrasolar giant planets have commonly been estimated by assuming they consist of two components: a blackbody spectrum of the primary reflected by a gray surface and a blackbody thermal emission. The spectra of all of the Jovian planets in our own solar system deviate widely from such a simple model. Thus it comes as no surprise that the model spectra for extrasolar planets also depart from such a simple picture.

In reflected light the planets do not resemble gray reflecting spheres. Instead their reflected spectrum is controlled by Rayleigh scattering and molecular absorption. In addition in the UV absorption by hazes and non-equilibrium photochemically-produced molecules will depresses the reflected flux. For all but the earliest spectral types (O and B) Raman scattering also lowers the albedo for wavelengths less than that of the peak stellar emission. As a consequence planets reflect most efficiently shortward of about  $0.6\,\mu\text{m}$  where photons can Rayleigh scatter before they are absorbed. At progressively longer wavelengths extrasolar giant planets become darker as Rayleigh scattering gives way to molecular absorption.

In the red and near-infrared planets are bright in reflected light only if there are clouds. Planets warmer than about 400 K will be dark in reflected light in the red and near-infrared and have relatively low Bond albedos. As the planet cools through about 400K, water clouds will appear, the planets will brighten, and the Bond albedo will increase, perhaps dramatically. The larger Bond albedo will then hasten the cooling of the planet as less incident stellar energy is absorbed. Some condensates will likely always be present in the warmer atmospheres (Guillot et al. 1997b). However all such condensates are of species substantially less abundant than water and will have a proportionately smaller influence on the reflected spectrum.

The great sensitivity of the geometric and Bond albedos to unconstrained model parameters means that it will only be possible to predict families of possible spectra for a given cloudy planet. The uncertainty is less for objects too warm to have condensed clouds or for cases where the cloud lies relatively deep in the atmosphere. The great range of possible cloud models shown in Figures 6 and 8 is partly a consequence of the high altitude of the water cloud in these particular cases.

This same sensitivity, however, will allow the construction of detailed atmosphere models once spectra are obtained of extrasolar giant planets. It will then be possible to study the physics of cloud formation in a large range of atmospheres.

The geometric albedo and phase integral spectra produced by this study can be combined with the emergent spectra of any primary star to generate an approximate reflected spectrum. Figures 10 and 11 demonstrate such a calculation for objects orbiting at 1 AU from a G2V primary. Again adding water clouds to the cooler produces a substantial brightening. The effect of silicate clouds is more subtle and is shown in Figure 11.

Burrows et al. (1997) demonstrated the emitted spectra of extrasolar giant planets are remarkably non-Planckian. The planets emit strongly in the windows in between strong methane and water absorption bands. Jupiter’s own five-micron window is an example of this process. Thermal emission spectra from the cloud-free models of Burrows et al. are also plotted on Figures 10 and 11. For the cloudy model, the thermal emission in the near-infrared model is comparable to the reflected flux. For even warmer objects, the thermal emission will dominate the reflected flux for objects at 1 AU and farther from their primaries. For cooler objects the reflection from bright clouds will swamp the rapidly falling near-infrared emission. For such objects a full radiative transfer treatment of the combined scattered and emitted radiation is clearly required.

The dominance of thermal emission for a hot planet at 1 AU is apparent in Figure 11. The reflected flux would be comparable to the thermal emission only for objects closer than about 0.1 AU to their primary. Hence the spectra of the 51 Peg B class of planets will be a mixture of reflected and emitted radiation. The relative importance of reflected incident radiation and thermal emission can be estimated from the type of the primary, the planetary Bond albedo, and the infrared flux.

A complete model of the reflected spectra of a cooling planet must thus include all condensates and self-consistently account for the deposition of incident radiation into the atmosphere. Given the great range in possible primaries and orbital distances, the dependence of Bond albedo upon the incident spectra, and the uncertainties inherent in cloud physics, the overall phase space within which models must be constructed is remarkably large.

We thank Robert West for a thorough and helpful review and K. Rages, T. Guillot, D. Saumon, and A. Burrows for helpful discussions. The authors acknowledge the support of the NASA Faculty Awards for Research (MM), Planetary Atmospheres (MM, RF), and Origins of Solar Systems (JL) programs as well as the NSF CAREER (MM) program.

## REFERENCES

Baines, K.H., Bergstralh, J.T. 1986, *Icarus*, 65, 406

- Baines, K. H., Smith, W.H., & Alexander, C. 1989, In *Time-Variable Phenomena in the Jovian System*, NASA SP-494 Eds. M. Belton, R. West, & J. Rahe, 363
- Barshay, S.S. & Lewis, J.S. 1976, ARA&A, 14, 81
- Belton, M.J.S., McElroy, M.B., & Price, M.J. 1971, ApJ, 164, 191
- Burrows, A. & Sharp, C. 1998, ApJsubmitted.
- Burrows, A., Marley, M., Hubbard, W.B., Lunine, J.I., Guillot, T., Saumon, D., Freedman, R., Sudarsky, D., & Sharp, C. 1997, ApJ, 491, 856
- Butler, R. P., & Marcy, G. W. 1996, ApJ, 464, L153
- Butler, R. P., Marcy, G. W., Williams, E., Hauser, H., & Shirts, P. 1997, ApJ, 474, L115
- Cochran, W. D., Hatzes, A. P., Butler, R. P., & Marcy, G. 1997, ApJ, 483, 457
- Conrath, B.J., Hanel, R.A., & Samuelson, R.E. 1989, In *Origin and Evolution of Planetary and Satellite Atmospheres*. Eds. S.K. Atreya, J.B. Pollack, & M.S. Matthews. Tucson, Univ. of Ariz. Press, 513
- Courtin, R.D., Gautier, D., & McKay, C.P. 1995, Icarus, 114, 144
- Dlugach, J.M. & Yanovitskij, E.G. 1974, Icarus, 22, 66
- Eisenberg, D. & Kauzmann, W. 1969. *The Structure and Properties of Water*. New York, Oxford Univ. Press
- Guillot, T., Marley, M., Saumon, D. & Freedman, R. 1997a, in *Infrared Space Interferometry: Astrophysics & the Study of Earth-like Planets*. Eds. C. Eiroa *et al.*, Kluwer Academic Publishers, Dordrecht, 37
- Guillot, T., Saumon, D., Burrows, A., Hubbard, W., Lunine, J., Marley, M., & Freedman, R. 1997b, in *Astronomical and Biochemical Origins and the Search for Life in the Universe*, eds. C. Cosmovici, S. Bowyer, & D. Werthimer, 343
- Gunn, J. E. & Stryker, L. L. 1983, ApJS, 52, 121
- Hanel, R., Conrath, B.J., Jennings, D.E., & Samuelson, R.E. 1992, *Exploration of the Solar System by Infrared Remote Sensing*, Cambridge, Cambridge Univ. Press
- Hudgins, D.M., Sandford, S.A., Allamandola, L.J. & Tielens, A.G.G.M. 1993, ApJS86, 713
- Karkoschka, E. 1994, Icarus, 111, 174
- Lang, K.R. 1992 *Astrophysical Data: Planets and Stars*. Springer-Verlag, 937 pp.
- Lindal, G.F., Lyons, J.R., Sweetnam, D.N., Eshleman, V.R., Hinson, D.P. & Tyler, G.L. 1987, JGR, 92, 14,987
- Lunine, J.I., Hubbard, W.B., Burrows, A., Wang, Y-P. & Garlow, K. 1989, ApJ., 338, 314
- Marcy, G. W., & Butler, R. P. 1996, ApJ, 464, L147
- Marley, M.S., Saumon, D., Guillot, T., Freedman, R, Hubbard, W., Burrows, A., & Lunine, J. 1996, Science, 272, 1919

- Marley, M.S. 1998, In *Brown Dwarfs and Extrasolar Planets* ASP Conference Series, R. Rebolo, E. Martin, and M. R. Zapatero Osorio (eds.), 134, 383
- Marley, M.S. & McKay, C.P. 1998, *Icarus*, submitted
- Mayor, M., & Queloz, D. 1995, *Nature*, 378, 355
- McKay, C.P., Pollack, J.B. & Courtin, R. 1989, *Icarus*, 80, 23
- Moses, J.I., Rages, K., & Pollack, J.B. 1995, *Icarus*, 113, 232
- Pollack, J.B., Rages, K., Baines, K.H., Bergstrahl, J.T., Wenkert, D. & Danielson, G.E. 1986, *Icarus*, 65, 442
- Pollack, J.B., Hubickyj, O., Bodenheimer, P., Lissauer, J.J., Podolak, M., & Greenzweig, Y. 1996, *Icarus*, 124, 62
- Rages, K., Pollack, J.B., Tomasko, M.G., & Dose, L.R. 1991, *Icarus*, 89, 359
- Rossow, W.V. 1978, *Icarus*, 36, 1
- Saumon, D., Hubbard, W.B., Burrows, A., Guillot, T., Lunine, J.I., & Chabrier, G. 1996, *ApJ*, 460, 993
- Savage, B.D. & Caldwell, J.J. 1974, *ApJ*, 187, 197
- Scott, A., & Duley, W.W. 1996, *ApJS*, 105, 401
- Strecker, D. W., Erickson, E. F. & Witteborn, F. C. 1979. *ApJS*, 41, 501
- Toon, O.B., McKay, C.P., Ackerman, T.P. & Santhanam, K. 1989, *J. Geophys. Res.*, 94, 16287



Fig. 1.— Geometric albedo spectrum for Jupiter and Uranus (Karkoschka 1994), compared to model spectra for a Jupiter-mass, solar-composition, planet with Jupiter’s effective temperature (128 K). The model spectra demonstrate the importance of clouds in controlling the reflected spectra. Both models have a solar abundance of methane and no water. The cloudy model includes a stratospheric haze at 0.001 bar (with an optical depth  $\tau = 0.1$ ) and a tropospheric cloud at 1 bar ( $\tau = 5$ ). Both condensate layers scatter conservatively and are gray. The characteristics of Jupiter’s clouds have been derived by varying the locations and optical properties to best fit the observed spectrum (e.g. Baines et al. 1989).

Fig. 2.— Model phase integral spectra for a  $12 M_J$  object with  $T_{\text{eff}} = 300 \text{ K}$ . Phase integral is primarily sensitive to scattering properties of clouds, which in turn depend upon particle size and composition.

Fig. 3.— (a) Water condensation and cloud size profile for a warm, Jupiter-mass planet with  $T_{\text{eff}} = 300 \text{ K}$  and  $g = 22 \text{ m sec}^{-2}$ . Shown are the model temperature profile and the condensed water vapor density. These quantities do not depend upon the cloud model. The particle size profile is shown for both a turbulent and a quiescent cloud. (b) Same as (a), but for silicate ( $\text{MgSiO}_3$ ) cloud and a hotter (Gliese 229 B - like) model with  $T_{\text{eff}} = 1000 \text{ K}$  and  $g = 1000 \text{ m sec}^{-2}$ .

Fig. 4.— Geometric albedo spectra for three models with  $T_{\text{eff}} = 128 \text{ K}$  and varying gravity. All three atmospheres are quite dark in reflected light beyond about  $0.6 \mu\text{m}$ . Note log geometric albedo scale.

Fig. 5.— Geometric albedo spectra for two model atmospheres, each with Jupiter’s gravity, but differing effective temperatures. The Jupiter-like model differs from that shown in Figure 1 by having a solar abundance of water below the condensation level. An ammonia band is apparent in the colder model near  $0.62 \mu\text{m}$ .

Fig. 6.— Geometric albedo spectra for cloud-free and water-cloud models with  $g = 22 \text{ m sec}^{-2}$  and  $T_{\text{eff}} = 300 \text{ K}$ . (a) Spectra of atmospheres with no cloud, turbulent cloud, and quiescent cloud. To clearly demonstrate the influence of the cloud model upon the spectra,  $f_s = 1$  is assumed. Particle sizes are smaller for the quiescent cloud which enhances the geometric albedo at the shortest wavelengths. In the near-infrared the greater column abundance of the smaller particles enhances scattering substantially for the radiative cloud. Both cloud models are much brighter than an atmosphere with no clouds. (b) Comparison of spectra assuming clouds with various supersaturation factors. For  $f_s = 0.01$  effect of cloud is only apparent beyond about  $1 \mu\text{m}$  where the 100-fold decrease in cloud particle column density translates into about a 10-fold drop in albedo which is nevertheless far brighter than for a cloud-free atmosphere (Figure 4). (c) Spectra for atmospheres with single particle size clouds, all with  $f_s = 0.01$ . Optical and near-IR scattering properties are similar for all cases with  $r_c \geq 10 \mu\text{m}$ .

Fig. 7.— Similar to Figure 6 but for silicate clouds in the atmosphere of a brown dwarf with

$T_{\text{eff}} = 1000 \text{ K}$ . and  $g = 1000 \text{ m sec}^{-2}$ . Model object, similar to G $\ell$ 229 B, has a mass of about  $36 M_{\text{J}}$ . The silicate clouds lower the albedo in the blue but are less detectable in the near-IR. (a) Comparison of cloud models with  $f_s = 1$ . (b) Effect of  $f_s$  on spectra. (c) Role of particle size.

Fig. 8.— Bond albedos for atmosphere with  $g = 22 \text{ m sec}^{-2}$  and  $T_{\text{eff}} = 300 \text{ K}$  and various model clouds as a function of the primary type. Symbols summarize cloud type, either turbulent, quiescent, or single-sized. Also shown (slightly offset for clarity) are the Bond albedos and associated uncertainties for Jupiter and Neptune (Conrath et al. 1989). (a) Models with  $f_s = 0.01$ . (b) Models with  $f_s = 0.1$ .

Fig. 9.— Similar to Figures 8 but for model with  $g = 1000 \text{ m sec}^{-2}$  and  $T_{\text{eff}} = 1000 \text{ K}$  and various  $\text{MgSiO}_3$  clouds. Note differing vertical scale from Figures 8.

Fig. 10.— Composite spectra for model with  $g = 300 \text{ m sec}^{-2}$  and  $T_{\text{eff}} = 300 \text{ K}$ . Lines, as indicated, show reflected spectra which would be measured at 10 pc from a planet orbiting at 1 AU from its primary. Long dashed line shows thermal emission from the same atmosphere model with no clouds as computed by Burrows et al. (1997). Reflected light dominates thermal emission in near-infrared for cloudy models with effective temperatures below this range. A number of photometric bandpasses are shown for reference.

Fig. 11.— As for Figure 10, but for a roughly  $36 M_{\text{J}}$  model with  $g = 1000 \text{ m sec}^{-2}$  and  $T_{\text{eff}} = 1000 \text{ K}$  and silicate clouds. Thermal emission dominates reflected flux for such hot models. For a planet orbiting inside of 0.1 AU, reflected flux would be comparable to emitted flux.

TABLE 2  
BOND ALBEDOS FOR CLOUDY PLANETS

$f_s$ <sup>1</sup>	Gravity m/s <sup>2</sup>	$T_{\text{eff}}$ K	Cloud Type <sup>2</sup>	A5V	F4V	F8V	Spectral Type		G0V	G2V	G8V	K4V	M2V
0.01	22	300	–	0.40	0.38	0.33	0.33	0.31	0.24	0.19	0.07		
		300	TW	0.40	0.38	0.33	0.33	0.31	0.24	0.19	0.07		
		300	QW	0.39	0.37	0.32	0.32	0.30	0.24	0.18	0.07		
		300	W 0.1	0.78	0.80	0.76	0.76	0.75	0.70	0.64	0.47		
		300	W 1	0.83	0.88	0.86	0.86	0.87	0.84	0.81	0.72		
		300	W 10	0.50	0.49	0.44	0.44	0.42	0.37	0.31	0.19		
		300	W 100	0.44	0.42	0.37	0.36	0.34	0.27	0.21	0.08		
	300	300	–	0.39	0.37	0.32	0.31	0.29	0.23	0.17	0.06		
		300	TW	0.39	0.37	0.31	0.31	0.29	0.23	0.17	0.06		
		300	QW	0.40	0.39	0.33	0.33	0.31	0.25	0.19	0.08		
		300	W 0.1	0.66	0.67	0.62	0.62	0.61	0.55	0.48	0.31		
		300	W 1	0.73	0.77	0.75	0.75	0.75	0.72	0.69	0.61		
		300	W 10	0.46	0.45	0.40	0.40	0.38	0.32	0.27	0.16		
		300	W 100	0.39	0.37	0.32	0.32	0.29	0.23	0.17	0.06		
	1000	1000	–	0.40	0.39	0.33	0.33	0.31	0.24	0.19	0.06		
		1000	TS	0.41	0.39	0.34	0.34	0.31	0.25	0.19	0.06		
		1000	QS	0.41	0.39	0.34	0.34	0.31	0.25	0.19	0.06		
		1000	S 0.1	0.48	0.47	0.41	0.40	0.38	0.31	0.24	0.09		
		1000	S 1	0.40	0.39	0.33	0.33	0.31	0.24	0.18	0.06		
		1000	S 10	0.41	0.40	0.34	0.34	0.31	0.25	0.19	0.06		
		1000	S 100	0.41	0.39	0.34	0.34	0.31	0.25	0.19	0.06		
0.1	22	300	–	0.40	0.38	0.33	0.33	0.31	0.24	0.19	0.07		
		300	TW	0.39	0.38	0.33	0.33	0.31	0.24	0.19	0.07		
		300	QW	0.50	0.49	0.44	0.44	0.42	0.35	0.29	0.16		
		300	W 0.1	0.86	0.90	0.87	0.87	0.87	0.83	0.78	0.63		
		300	W 1	0.93	0.99	0.98	0.97	0.98	0.96	0.93	0.84		
		300	W 10	0.78	0.81	0.79	0.79	0.79	0.76	0.72	0.60		
		300	W 100	0.49	0.48	0.43	0.43	0.41	0.35	0.29	0.16		
	300	300	–	0.39	0.37	0.32	0.31	0.29	0.23	0.17	0.06		
		300	TW	0.44	0.43	0.38	0.37	0.35	0.29	0.24	0.12		
		300	QW	0.51	0.51	0.46	0.46	0.44	0.38	0.32	0.20		
		300	W 0.1	0.84	0.88	0.85	0.84	0.84	0.80	0.74	0.60		
		300	W 1	0.90	0.97	0.95	0.95	0.96	0.95	0.92	0.83		
		300	W 10	0.63	0.65	0.61	0.61	0.60	0.56	0.51	0.41		
		300	W 100	0.45	0.44	0.39	0.39	0.37	0.31	0.25	0.14		
	1000	1000	–	0.40	0.39	0.33	0.33	0.31	0.24	0.19	0.06		
		1000	TS	0.41	0.39	0.33	0.33	0.31	0.24	0.19	0.06		
		1000	QS	0.39	0.38	0.32	0.32	0.30	0.24	0.18	0.06		
		1000	S 0.1	0.51	0.51	0.46	0.46	0.44	0.38	0.31	0.16		
		1000	S 1	0.43	0.42	0.37	0.37	0.35	0.28	0.22	0.09		
		1000	S 10	0.39	0.37	0.32	0.32	0.30	0.23	0.18	0.06		
		1000	S 100	0.41	0.39	0.33	0.33	0.31	0.24	0.19	0.06		

<sup>1</sup>Supersaturation factor.

<sup>2</sup>– = No Cloud, T = Turbulent, Q = Quiescent, S = Silicate (MgSiO<sub>3</sub>), W = Water (H<sub>2</sub>O). A number indicates the radius of the particle (in  $\mu\text{m}$ ) for cloud models with a constant particle size.

